Published in "Physical Review A 82(6): 063408, 2010"
which should be cited to refer to this work.

Double K-shell photoionization and hypersatellite x-ray transitions of $12 \leqslant Z \leqslant 23$ atoms

J. Hoszowska,* J.-Cl. Dousse, W. Cao, K. Fennane, Y. Kayser, and M. Szlachetko
Department of Physics, University of Fribourg, CH-1700 Fribourg, Switzerland

J. Szlachetko†
European Synchrotron Radiation Facility (ESRF), F-38043, Grenoble, France

M. Kavčič
J. Stefan Institute, SI-1001, Ljubljana, Slovenia

Single-photon double K-shell ionization of low-Z neutral atoms in the range $12 \leqslant Z \leqslant 23$ is investigated. The experimental method was based on measurements of the high-resolution $K\alpha^h$ hypersatellite x-ray spectra following the radiative decay of the K-shell double-vacancy states excited by monochromatic synchrotron radiation. The photon energy dependence of the double K-shell ionization was measured over a wide range of photon energies from threshold up to and beyond the maximum of the double-to-single photoionization cross section ratios. From the high-resolution x-ray emission spectra the energies and linewidths of the hypersatellite transitions, as well as the $K\alpha_1^h$:$K\alpha_2^h$ intensity ratios, were determined. The relative importance of the initial-state and final-state electron-electron interactions to the K-shell double photoionization is addressed. Physical mechanisms and scaling laws of the K-shell double photoionization are examined. A semiempirical universal scaling of the double-photoionization cross sections with the effective nuclear charge for neutral atoms in the range $2 \leqslant Z \leqslant 47$ is established.

I. INTRODUCTION

The K-shell double photoionization (DPI) of neutral elements produces K-shell hollow atoms, i.e., atoms with an empty innermost shell and occupied outer shells. Because an incident photon interacts with a single electron, the ejection of two 1s electrons is driven by many-electron interactions. As electron correlation effects lie in the heart of understanding atomic structure, single-photon double ionization has received a great deal of interest both theoretically and experimentally [1–4]. Yet an accurate theoretical treatment of electron correlations in many-electron systems is far from complete and remains a challenge.

The radiative decay of the K-shell doubly ionized states results in x-ray transitions, named *hypersatellites* by Briand [5]. In fact, the first observation of hypersatellites was reported much earlier in 1953 by Charpak [6]. In these pioneering experiments the double 1s vacancies were created following nuclear K-shell electron capture of radioactive isotopes and the K-shell hypersatellites were measured by means of the satellite-hypersatellite coincidence technique. The hypersatellite transitions permit investigation of the double-ionization processes and also give insight into such fundamental aspects of atomic physics as the Breit interaction, quantum electrodynamics (QED), and relativity effects.

With the advent of intense and energy-tunable x-ray synchrotron sources, K-shell hollow atoms have drawn renewed interest experimentally and theoretically alike. Specifically, experimental investigation of the photon energy dependence of DPI in neutral atoms became accessible. So far, experimental results for the DPI cross-section ratios far beyond the broad maximum are available only for He [7] and Li [8]. Due to the low probability ($\sim 10^{-2}$–10^{-6}) for creating double K-shell vacancies in single-photon impact and the fast $\sim Z^{-4}$ decrease of the DPI cross sections, experiments are quite challenging and thus data are scarce. Hitherto, for atoms in the range $10 < Z < 20$ only few experimental data have been reported. Measurements with conventional x-ray sources were performed for Mg [9] and Ar [10]. The double K-shell ionization of Ne was investigated at a photon energy of 5 keV by means of high-resolution Auger electron spectroscopy [11]. However, to the best of our knowledge, the photon energy dependence of DPI in this Z range has not been determined. To date, the most extensive K x-ray hypersatellite studies have been carried out for the 3d transition metals. The double-to-single photoionization ratios were measured as a function of the incident photon energy from the DPI threshold to the broad maximum for Ca, Ti, and V [12], and for elements in the $23 \leqslant Z \leqslant 30$ range [13,14]. For mid-Z atoms, the photon energy dependence of the double K-shell production was investigated for Ag ($Z = 47$) [15] in the 50–90 keV range employing the satellite-hypersatellite coincidence method. Data for the double-to-single photoionization ratios at a single photon energy are also available for Mo ($Z = 42$) [15] and Zr ($Z = 40$) [16].

On the theoretical side, He and heliumlike ions have attracted considerable interest (see, e.g., [17–23]), but much less effort has been devoted to the DPI of neutral atoms. The single-photon double photoionization of neutral atomic targets was addressed within lowest-order perturbation theory (LOPT) [23]. A systematic study of the K-shell DPI of Be, Mg, and Ca using an *ab initio* nonperturbative approach was performed by Kheifets *et al.* [24]. Comparison with experimental data

*joanna.hoszowska@unifr.ch
†Also at Institute of Physics, Jan Kochanowski University, 25-406 Kielce, Poland.

shows difficulties of such *ab initio* calculations and the need for further theoretical efforts. On the other hand, semiempirical approaches complement our understanding of the K-shell double photoionization of many-electron systems. In our recent study [25], the issue of the relative importance of the initial-state correlations and final-state electron-electron interaction to the K-shell DPI was addressed. We have found that the *postphotoabsorption* electron-electron correlation is different for neutral atoms and He-like ions.

This work is a continuation of efforts in the endeavor of bringing additional insights to electron-electron interactions and in understanding the double photoionization in many-body systems. To this end, the photon energy evolution of the double-to-single photoionization cross-section ratios for Mg, Al, Si, Ca, Sc, and V in a wide photon energy range and at a single energy for Cl and K were determined. Energies and linewidths of the $K\alpha^h$ ($1s^{-2} \rightarrow 1s^{-1}2p^{-1}$) hypersatellite x-ray transitions, and the $K\alpha_1^h$:$K\alpha_2^h$ intensity ratios are reported and compared to theoretical calculations as well as to other available experimental data. The double K-shell photoionization of low-Z atoms is investigated along the lines presented in our recent work [25]. The Z-dependent trends and scaling properties of the double-to-single photoionization cross-section ratios and the DPI cross sections are examined.

II. EXPERIMENT AND DATA ANALYSIS

A. Experimental method

The experiments were performed at the European Synchrotron Radiation Facility (ESRF), using monochromatic, energy-tunable synchrotron radiation and the Fribourg von Hamos Bragg-type curved crystal x-ray spectrometer [26]. The experimental method was based on measurements of the high-resolution hypersatellite x-ray spectra following the radiative decay of the K-shell double-vacancy states. The double-to-single photoionization cross-section ratios P_{KK} were obtained from the relative intensities of the resolved hypersatellite $K\alpha^h$ ($1s^{-2} \rightarrow 1s^{-1}2p^{-1}$) to the diagram $K\alpha$ ($1s^{-1} \rightarrow 2p^{-1}$) x-ray transitions:

$$P_{KK} = \frac{I_{K\alpha^h}}{I_{K\alpha}} \frac{\omega_K}{\omega_{KK}}, \tag{1}$$

where ω_K and ω_{KK} are the fluorescence yields for the single- and double-hole states [27], respectively. High-energy resolution was mandatory because the Mg, Al, and Si K hypersatellites are partly or completely overlapping with the L- satellites of the diagram $K\beta$ ($1s^{-1} \rightarrow 3p^{-1}$) lines, and in the case of Cl, K, and Ca the $K\alpha$ hypersatellites need to be resolved from the close-lying *KMM* radiative Auger transitions [28,29]. To probe the evolution of the double-to-single photoionization cross-section ratios over wide photon beam energy ranges up to ~3 times the DPI threshold energies, the measurements of the K hypersatellite and diagram x-ray transitions were carried out at two undulator beamlines (ID21 and ID26), and at a bending magnet beamline (BM5). The following photon beam energy ranges were covered: 2.746 to 8.0 keV for Mg, 3.122 to 7.0 keV for Al, 3.6 to 10.0 keV for Si, 8.5 to 28 keV for Ca, 9.4 to 28 keV for Sc, and 13.3 to 28 keV for V. Only the Cl and K data were collected at a single photon energy of 13.3 keV in the region of the broad maximum of the double-to-single photoionization cross-section ratios.

A detailed description of the Fribourg von Hamos Bragg-type curved crystal x-ray spectrometer can be found in Refs. [26,30]. Thus, in the following only the spectrometer operational characteristics related to the experiments will be outlined. The principal elements of the spectrometer are an effective x-ray source, a crystal bent cylindrically to a nominal radius of 25.4 cm, and a position-sensitive detector, located on the crystal axis of curvature. The von Hamos geometry permits, at one positioning of the elements, data collection over an energy bandwidth limited primarily by the detector length. The effective x-ray fluorescence source viewed by the crystal is usually defined by a rectangular slit with an adjustable width. Alternatively, the effective source size may be defined by a focused beam spot on the sample, and the slit is left wide open. This so-called slitless operation mode results in a higher overall detection efficiency. The sample, crystal, and detector are all contained in an evacuated stainless steel chamber equipped with several beam ports. In the standard geometry the angle between the beam direction and the crystal axis of curvature is 90°. By rotating the chamber by 180°, the spectrometer can be operated in the so-called inverse geometry. In the present experiments four different crystals were mounted, namely, a thallium acid phthalate TlAP(001) ($2d = 25.772$ Å), an ammonium dihydrogen phosphate ADP(101) ($2d = 10.642$ Å), a LiF(200) ($2d = 4.028$ Å), and a Ge(200) ($2d = 4.000$ Å) crystal. The diffracted x rays were recorded with a thermoelectrically cooled (−45 to −50 °C) back-illuminated charge coupled device (CCD) camera consisting of 1340 columns and 400 rows with a pixel size of 20×20 μm^2. By setting appropriate energy windows, the CCD detector allows discrimination against higher-order crystal reflections and also a rejection of background events.

At the x-ray microscopy beamline ID21 the spectrometer was installed downstream of the scanning transmission x-ray microscope chamber to which it was connected by means of an evacuated pipe. Monochromatic photon beams with ~10 eV bandwidth were obtained using the double Ni-B_4C multilayer monochromator and the Ni-coated mirror served for upper harmonics rejection. The beam size was defined by means of a 1-mm-diam pinhole. The x-ray emission spectra of Mg were measured with the TlAP(001) crystal in second order and those of Al with the ADP(101) crystal in first order of reflection. The spectrometer slit width was set to 0.2 mm. Although a narrower width would result in a higher energy resolution, a loss in the detection efficiency would follow. Self-supported 3.3-μm- and 1-μm-thick metallic foils of Mg and Al, respectively, were used. To minimize self-absorption, the samples were tilted to the median angles between the incident beam direction and the direction of observation defined by the Bragg angles.

For the measurements at the BM5 beamline, the spectrometer was installed in the first experimental hutch and due to lack of space it was operated in the inverse geometry. The primary x-ray beam was monochromatized by means of a [Ru-B_4C]$_{70}$ double-multilayer monochromator with $\Delta E/E \sim 2 \times 10^{-2}$ and the harmonics rejection rate of 1.8×10^{-4} in the 6 to 30 keV photon energy range. The beam size on the sample was defined by means of a 2-mm-high and 5-mm-wide

rectangular slit placed in front of the spectrometer beam port. The spectrometer was equipped with the ADP(101) crystal for the x-ray spectra measurements of K and Cl, and the LiF(200) crystal for Ca and V. A self-supported 40-μm-thick metallic foil of V, a 0.4-mm-thick KCl crystal, and a 0.115-mm-thick Ca sample were used. Each sample was tilted to the respective median angle.

At the ID26 beamline, for photon energies up to 16 keV the Si(111) double-crystal monochromator was employed, whereas for higher energies the Si(311) crystals were used. Depending on the photon energy, the double Si-coated, Cr- and Pd-coated, and double Pt-coated mirrors suppressed the upper harmonics. The mirrors served also to focus the beam horizontally on the sample to $\sim$250 μm, thereby permitting operation of the spectrometer in the slitless geometry. An evacuated pipe was used to connect the spectrometer to the beamline. Self-supported metallic foils of Mg (50 μm thick), Al (1.5 μm thick), Sc (25 μm thick), and V (40 μm thick) were employed. The *c*-Si sample was 1 mm thick and the Ca target thickness was 0.084 mm. The samples were mounted perpendicularly to the incident beam.

The incident photon flux was $\sim(1\text{–}3)\times10^{12}$ photons/s at the three beamlines. The time of a single acquisition was chosen depending on the count rate. The acquisition times for the diagram x-ray transitions were 1 s/image, and to avoid multiple-hit events on one pixel the photon flux was attenuated with appropriate absorbers. The hypersatellite x-ray spectra were collected in short successive scans of a few hundred CCD images with acquisition times of 2–10 s per image. For the x-ray hypersatellite spectra of Cl, K, and Ca, two or three overlapping CCD regions were measured to include the *KMM* radiative Auger transitions and $K\beta$ diagram lines. For normalization purposes, the photon number was determined with a photodiode at the beginning and the end of each x-ray emission spectrum measurement. This allowed us to monitor the photon flux and to correct the x-ray spectra offline for any beam intensity fluctuations.

B. Data analysis

For the studied elements, the $K\alpha_2^h$ hypersatellite ($^1P_1\rightarrow{}^1S_0$) was predominant, the spin-flip $K\alpha_1^h$ transition ($^3P_1\rightarrow{}^1S_0$) being forbidden by the $E1$ selection rule in the L-S coupling scheme that prevails for low-Z elements. The x-ray emission spectra were calibrated using several K- and L-diagram transitions for which energies reported in Ref. [31] were assigned. The following fluorescence lines were used: for the Mg sample, the Mg $K\alpha$ and Se $L\beta_1$; for Al, the Al $K\alpha$, Si $K\alpha$, and $L\beta_1$ of Ag measured in second order of diffraction; for Si, the Si $K\alpha$ and Al $K\alpha$; for Cl, the Cl $K\alpha$ and Rh $L\beta_1$; for K, the Sb $L\alpha_1$ and K $K\beta$; for Ca, the Sb $L\beta_1$ and Ca $K\beta$; for Sc, the $K\alpha$ and $K\beta$ of Ca and Sc; and for V, the $K\alpha$ and $K\beta$ of V. These energy calibration measurements served also to determine the instrumental response function and the energy resolution of the spectrometer. The fluorescence x-ray spectra were analyzed by means of a least-squares fitting program. Voigt or Lorentzian functions were used, where the Voigt profile results from the convolution of a Lorentzian, representing the intrinsic x-ray line shape, with a Gaussian experimental response function. To determine the instrumental broadening

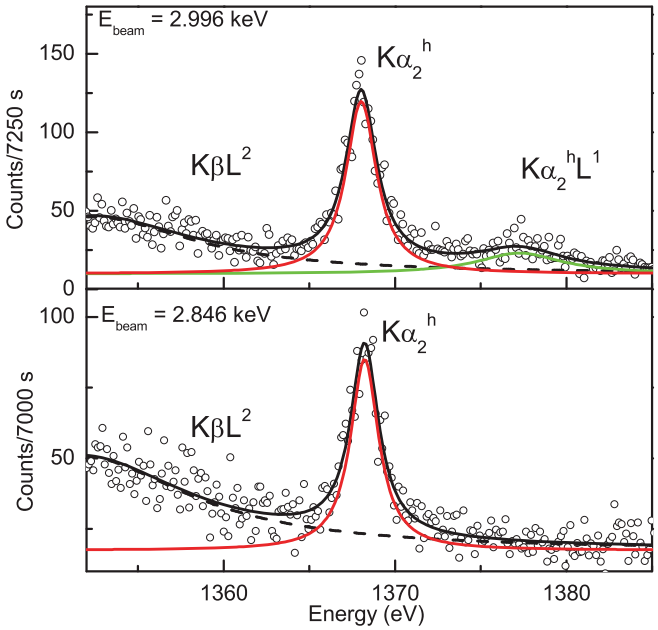

FIG. 1. (Color online) K-hypersatellite x-ray emission spectra of Mg measured at a photon beam energy just above the K-shell double-ionization threshold and in the region of the DPI cross-section maximum (2.996 keV). The red solid line corresponds to the $K\alpha_2^h$ hypersatellite, the green solid line to the $K\alpha_2^hL^1$ hypersatellite satellite, and the black dashed line to the $K\beta L^2$ satellite.

the Lorentzian widths were deduced from the recommended level widths of Campbell and Papp [32] and kept fixed in the fits. The instrumental broadening was found to be well reproduced by Gaussian profiles with full widths at half maximum (FWHM) ranging from 0.75 to 2.4 eV. Only in the case of the Mg x-ray spectra was the instrumental response of the spectrometer Lorentzian with a width of 0.54 eV. The overall energy resolution of the experimental setup was comparable to the natural linewidths of the measured x-ray transitions. The $K\alpha_2^h$ hypersatellite transitions were fitted with all parameters left free except the Gaussian widths. In the case of the very weak $K\alpha_1^h$ transitions, for all elements with the exception of V, the Lorentzian widths had also to be kept fixed in the fit (see Sec. III B).

For illustration, the Mg x-ray emission spectrum collected at two different incident photon energies is shown in Fig. 1. On the low-energy side of the $K\alpha_2^h$ transition, the high-energy component of the $K\beta L^2(K^{-1}L^{-2}\rightarrow L^{-2}M^{-1})$ satellite can be seen. The K hypersatellite spectrum measured at the beam energy of 2.996 keV is also accompanied by the first-order L satellite of the hypersatellite $K\alpha_2^hL^1$ resulting from the presence of an L-shell vacancy during the x-ray emission. The upward energy shift of the $K\alpha_2^hL^1$ transition is due to the reduced screening. For Al, the $K\beta L^2$ satellite transitions overlap with the $K\alpha^h$ x-ray hypersatellite spectrum, making the data analysis more complicated [33]. In turn, the Si hypersatellite x-ray spectrum is affected by the first-order $K\beta L^1$ satellite components shown in the lower panel of Fig. 2. By tuning the beam energy below the DPI threshold, the energy, widths, and relative intensities of the three Voigt components of the $K\beta L^1$ spectrum were determined and kept fixed in the fits of the Si hypersatellite spectra (see Fig. 2). In

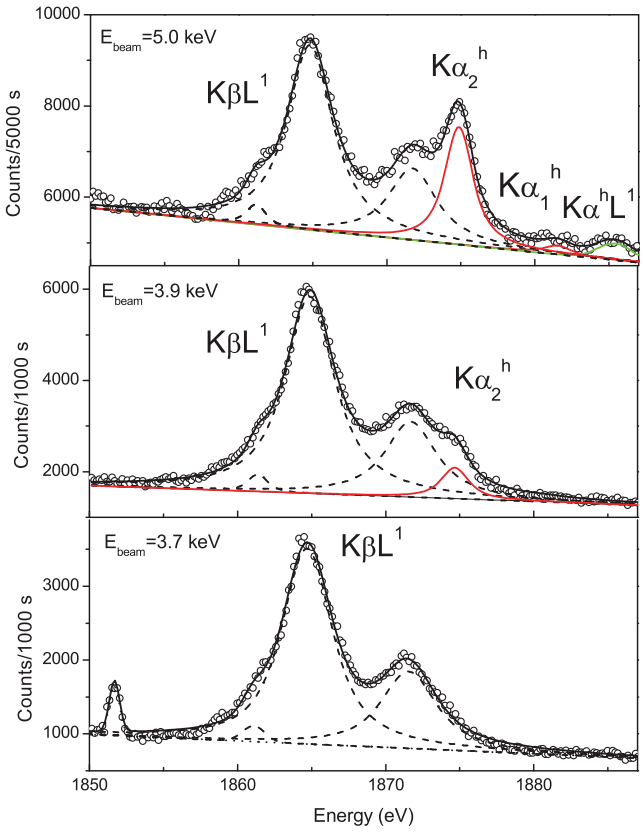

FIG. 2. (Color online) Si hypersatellite $K\alpha_2^h$ and $K\alpha_1^h$ spectra (red solid lines) measured at the indicated photon beam energies and the $K\beta L^1$ satellite spectrum (black dashed lines). The green solid line depicts the $K\alpha^h L^1$ satellite. The line at 1.851 keV (lower panel) corresponds to the elastic scattering peak of 3.7 keV photons in the second diffraction order.

the upper panel is shown the Si spectrum measured at a beam energy in the region of the maximum of the DPI cross section. Both the $K\alpha_2^h$ and $K\alpha_1^h$ transitions are observed, as well as the accompanying L satellite.

In the analysis of the K, Cl, and Ca x-ray spectra depicted in Fig. 3 special care had to be taken to account properly for the close-lying transitions originating from the *KMM* radiative Auger effect (RAE) and the low-energy tails of the $K\beta$ diagram lines. In the radiative Auger effect an inner-shell vacancy decays by a simultaneous emission of a photon and an electron. The *KMM* radiative Auger transition is a double-electron transition in which an M-shell electron fills the K-shell vacancy and another M-shell electron is simultaneously excited to a bound or a continuum state. As the energy is shared between the electron and the emitted photon, the *KMM* radiative Auger effect results in spectral features on the low-energy side of the $K\beta$ diagram line. Thanks to the high resolution, the main components could be resolved and thereby several Voigt profiles were sufficient to fit the *KMM* broad structure. As shown in Fig. 3, the $K\alpha_2^h$ and $K\alpha_1^h$ lines of Ca are quite well separated from the *KMM* transitions. Likewise, the RAE structure of K only partly overlaps with the $K\alpha_2^h$ hypersatellite. In contrast, a considerable number of the low-energy *KMM* RAE transitions coincide with the Cl K x-ray hypersatellites. Thus, to fit the Cl hypersatellite transition the shape of the *KMM* profile had to be determined. To circumvent this difficulty, the RAE of Cl was measured in house, employing the same high-resolution x-ray crystal spectrometer and an electron gun. Because of the insulating character of the KCl crystal, an NaCl sample, made from NaCl crystallites dusted on an Al support, was used instead. The shape of the low-energy *KMM* profile could be well reproduced by two asymmetric logistic functions, whose parameters were then kept fixed in the fit of the Cl hypersatellite spectrum. For Sc and V, as can be observed in Fig. 4, the $K\alpha_2^h$ and $K\alpha_1^h$ hypersatellites were well resolved, and the analysis was straightforward.

The hypersatellite and diagram line intensities were corrected for the differences in the sample self-absorption and absorption of the incident x rays, the photon flux, the spectrometer solid angle, and the crystal reflectivity, as well as for the detector quantum efficiency. For the fluorescence yield ratios relative uncertainties of 5% were assumed. The total correction factors varied typically from 0.8 to 1.2 depending on the experimental setup parameters and x-ray transition energies.

III. HYPERSATELLITE RADIATIVE TRANSITIONS

A. Energies

The obtained $K\alpha_1^h$ and $K\alpha_2^h$ hypersatellite energies as well as the $E_{K\alpha_1^h} - E_{K\alpha_2^h}$ energy splittings are summarized in Table I. Our results are compared to the few existing data for low-Z elements and the most recent theoretical calculations from Martins *et al.* [34], Costa *et al.* [35], and Natarajan [36]. Since Costa *et al.* [35] present energy shifts relative to the corresponding diagram lines, the listed $K\alpha_1^h$ and $K\alpha_2^h$ transition energies were calculated using the recommended values of Deslattes *et al.* [31] for the $K\alpha_1$ and $K\alpha_2$ lines. The energies of the $K\alpha_2^h$ hypersatellite transitions for Mg and Si are in very good agreement with the multiconfiguration Dirac-Fock (MCDF) calculations of Costa *et al.* [35] and those of Natarajan [36], as well as with other available experimental data. For Al, the calculated energy is slightly higher than our result, but the values are consistent within the combined error [33]. At higher Z, theory underestimates the experimental energies for both the $K\alpha_2^h$ and $K\alpha_1^h$ lines. The values for the $K\alpha_2^h$ energies agree within ~1.5 eV, except for Cl where theory deviates by ~2.8 eV from our experimental result. The differences are found to be greater for the $K\alpha_1^h$ hypersatellite. The estimated uncertainty of the theoretical transition energies is of the order of 1 eV. In general, the predictions of Costa *et al.* [35] are closer to our results than those of Martins *et al.* [34] and Natarajan [36]. For V the listed experimental values are consistent within ~1 eV, while for Ca the measured $K\alpha_2^h$ energy of Oura *et al.* [12] deviates from our result by 4 eV. The present $E_{K\alpha_1^h} - E_{K\alpha_2^h}$ energy splittings are somewhat greater than the calculated values, but agree within the combined experimental and theoretical errors.

B. Linewidths

The width Γ of an excited atomic state is related to the mean lifetime τ of the vacancy by the Heisenberg uncertainty relation $\Gamma\tau = \hbar$. This finite lifetime gives to an x-ray transition line a Lorentzian shape with a natural width equal to the

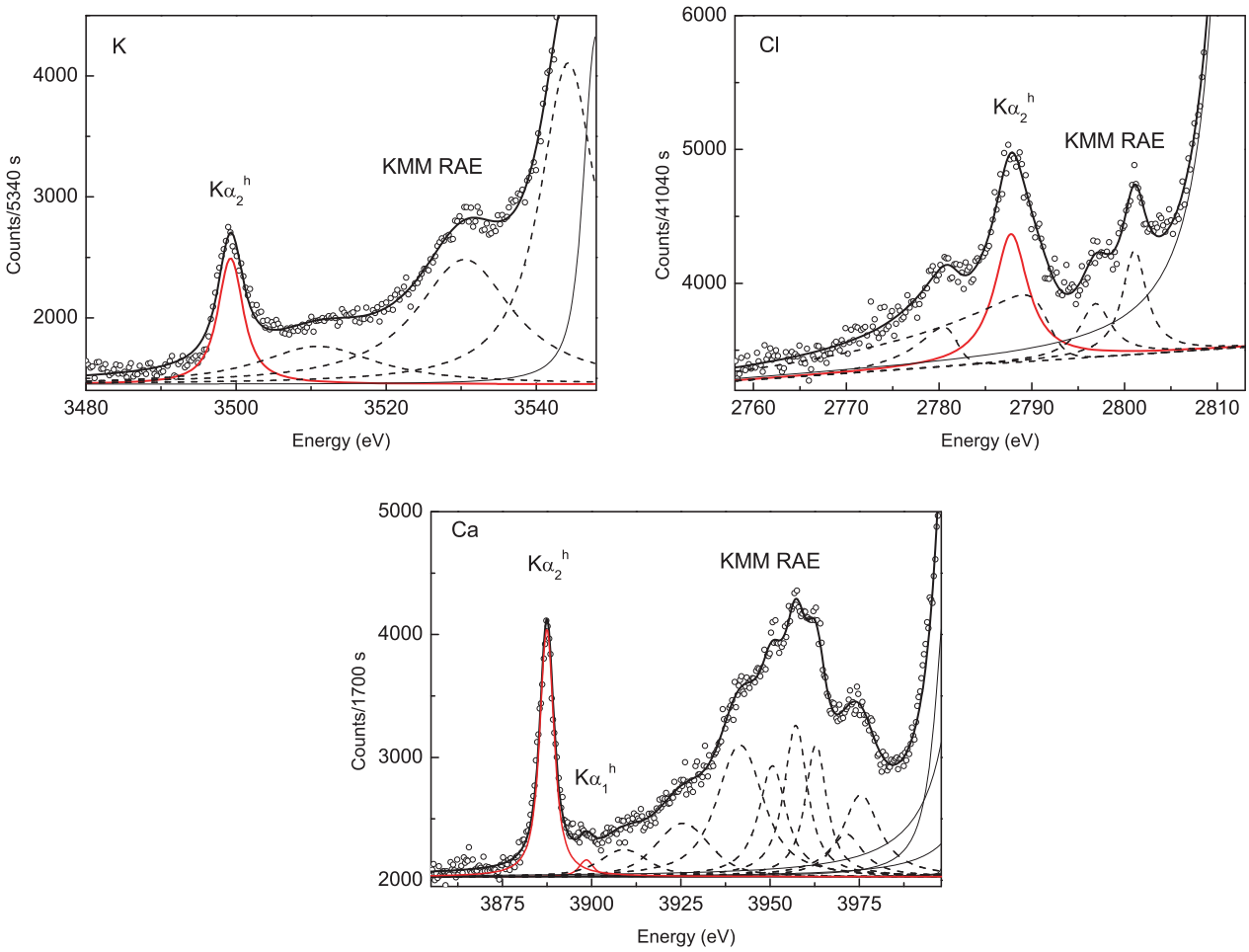

FIG. 3. (Color online) The Cl, K, and Ca hypersatellite spectra (red solid lines) and the accompanying *KMM* radiative Auger structures (black dashed lines). The Cl and K spectra were collected at an incident beam energy of 13.3 keV and for Ca the beam energy was 17.7 keV. The thin black solid lines correspond to the low-energy tails of the $K\beta_{1,3}$ x-ray transitions.

sum of the total radiative and radiationless widths of the initial and final states involved in the transition. For the K hypersatellite transition, the linewidth is given by the sum of the total widths of the initial $1s^{-2}$ and final $1s^{-1}2p^{-1}$ double-hole configuration states. Mossé *et al.* [39] suggested that the K hypersatellite linewidth can be approximated by the sum of atomic level widths $2\Gamma_K + (\Gamma_K + \Gamma_L)$. Diamant *et al.* [40] proposed a slightly modified expression

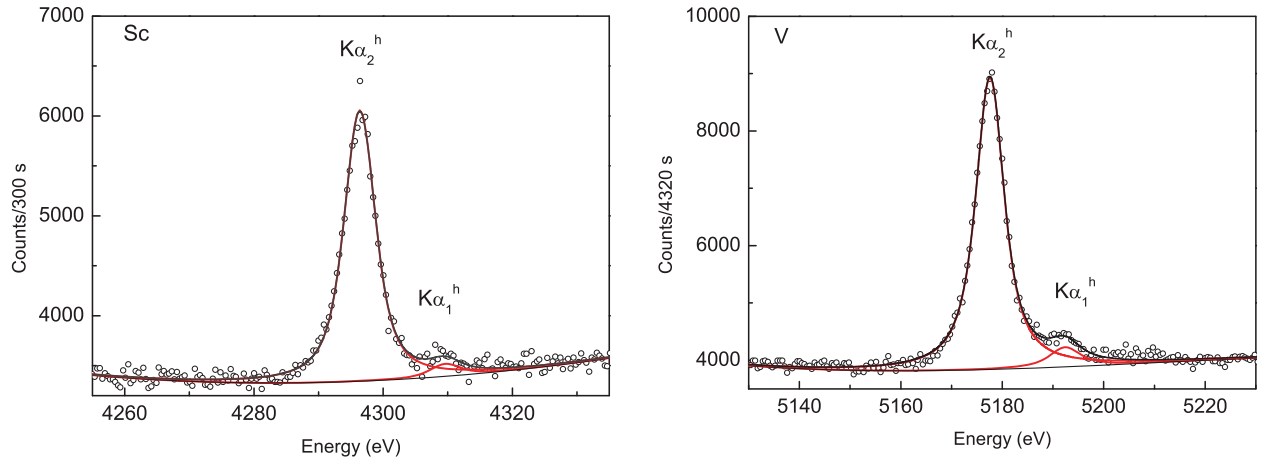

FIG. 4. (Color online) High-resolution K hypersatellite spectra of Sc and V measured at photon beam energies 14.0 and 17.7 keV, respectively. The red solid lines correspond to the $K\alpha_2^h$ and $K\alpha_1^h$ hypersatellites.

TABLE I. Hypersatellite energies and the $E_{K\alpha_1^h} - E_{K\alpha_2^h}$ energy splitting compared to other experimental data and theoretical predictions. The notation 1367.86(9/6) means 1367.86 ± 0.09 eV with an included statistical error from the fit of 0.06 eV.

	$K\alpha_2^h$ (eV)				$K\alpha_1^h$ (eV)				$E_{K\alpha_1^h} - E_{K\alpha_2^h}$ (eV)	
		Theory				Theory				Theory
Element	Experiment	[34]	[35]	[36]	Experiment	[34]	[35]	[36]	Experiment	[35]
Mg	1367.86(9/6)	1368.53	1367.71	1367.7						
	1367.8(2)[a]									
	1367.7(6)[b]									
Al	1610.38(4/2)	1611.75	1610.89							
Si	1874.87(6/4)	1874	1873.99	1874.5	1881.20(12/8)	1880	1879.96	1881.6	6.33(13)	5.96
	1873.6(1)[c]									
Cl	2787.80(10/8)	2785								
K	3499.20(9/6)	3498	3497.77							
Ca	3887.50(9/5)	3884.8	3885.93	3884.5	3899.80(15/9)	3896.39	3897.54	3896.3	12.30(17)	11.59
	3883.5(6)[d]									
Sc	4296.31(8/7)	4294.16	4295.24		4309.6(7/6)	4306.27	4307.43		13.29(11)	12.11
V	5177.65(8/6)	5174	5176.24		5192.0(9/7)	5188	5190.86		14.35(12)	14.51
	5178.1(5)[d]									
	5176.6(1)[e]				5191.7(1)[e]				15.1(1)[e]	

[a]Mikkola *et al.* [37].
[b]Keski-Rahkonen *et al.* [9].
[c]Kavčič and Tökési [38].
[d]Oura *et al.* [12].
[e]Diamant *et al.* [14].

$(\Gamma_{KK^{-1}} + \Gamma_K)$+$(\Gamma_K + \Gamma_L^{Z+1})$, where $\Gamma_{KK^{-1}}$ is the transition rate per K vacancy for the double-K-hole state and Γ_L^{Z+1} is the L-shell level width in the $(Z+1)$-approximation model. Indeed, for low-Z elements the $\Gamma_{KK^{-1}}$ widths are larger than the level widths Γ_K corresponding to the single-K-hole states [27,36]. Furthermore, since the K level width in the presence of the L-shell spectator vacancy $\Gamma_{KL^{-1}}$ is reduced [38,41,42], $\Gamma_{K\alpha^h}$ is rather given by

$$\Gamma_{K\alpha^h} = \Gamma_{KK} + (\Gamma_{KL^{-1}} + \Gamma_L), \tag{2}$$

where $\Gamma_{KK} = 2\Gamma_{KK^{-1}}$. Present experimental $\Gamma_{K\alpha^h}$ linewidths are summarized in Table II and compared to the values calculated using Eq. (2). For illustration, the measured and calculated $\Gamma_{K\alpha_2^h}$ linewidths along with the particular single- and double-vacancy level widths are depicted in Fig. 5(a). The widths Γ_{KK} and Γ_K were obtained by interpolating the values corresponding to the atomic numbers selected by Chen [27]. The accuracy of the interpolation procedure is at the level of ∼1%–4%. The $\Gamma_{KL^{-1}}$ widths were estimated following the scaling procedure of Larkins [41] and using for the radiative and Auger K level widths the interpolated values from Chen [27]. For the Γ_L, the recommended values of Campbell and Papp [32] were adopted. The Γ_L error estimates are 30% for $Z \leqslant 20$ and 10%–30% for $20 \leqslant Z \leqslant 40$.

For elements in the $12 \leqslant Z \leqslant 30$ range the calculated values systematically underestimate the experimental linewidths by ∼13% to 44%. The difference is only 0.2 eV at $Z = 12$, but amounts to as much as 2.0 eV at higher Z. These discrepancies

TABLE II. Hypersatellite linewidths and the $I_{K\alpha_1^h}/I_{K\alpha_2^h}$ intensity ratios.

	$\Gamma_{K\alpha_2^h}$ (eV)		$\Gamma_{K\alpha_1^h}$ (eV)		$I_{K\alpha_1^h}/I_{K\alpha_2^h}$	
Element	Experiment	Calculated[a]	Experiment	Calculated[a]	Experiment	Theory [35]
Mg	1.49(8)	1.32				0.00074
Al	1.88(7)	1.47				0.0087
Si	1.86(9)	1.63	1.86[b]		0.03(1)	0.0288
Cl	2.86(34)	2.16				
K	3.46(22)	2.57				0.0189
Ca	3.72(18)	2.76	3.72[b]	2.76	0.035(13)	0.0274
Sc	3.88(17)	3.08	3.75[b]	2.95	0.045(9)	0.051
V	5.54(19)	3.86	5.61(1.0)	3.36	0.077(15)	0.0989
	5.5(1)[c]		6.0(6)[c]		0.08(1)[c]	

[a]Calculated from Eq. (2) in the text.
[b]Fixed in the spectral fit.
[c]Diamant *et al.* [14].

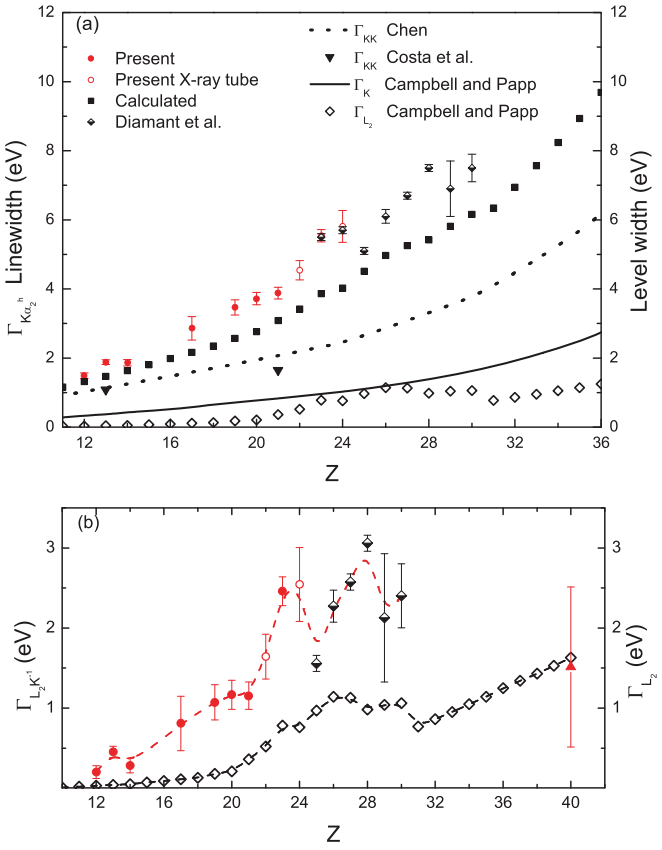

FIG. 5. (Color online) (a) Experimental hypersatellite $K\alpha_2^h$ linewidths (on the left y axis) compared to the calculated values (see text) and other experimental data of Diamant *et al.* [14] as a function of Z. On the right y axis shown are the theoretical total level widths Γ_{KK} of Chen [27] and Costa *et al.* [35]. Γ_K and Γ_{L_2} correspond respectively to the level widths K and L_2 recommended by Campbell and Papp [32]. (b) The $\Gamma_{L_2K^{-1}}$ widths (see text for details) compared to the Γ_{L_2} values [32]. Symbols are the same as in (a) and the dashed lines serve to guide the eye. X-ray tube data for Cr and Ti are from [43], and for $Z = 40$ from Boschung *et al.* [44].

may be partly due to non-lifetime-broadening effects such as the complex multiplet structure of the x-ray spectra resulting from the multiconfiguration states and multiple vacancies, and also to the multiplet splitting due the exchange interaction between the core holes and the incomplete valence shells. From the very good quality of the fits of the relativistic multiconfiguration Dirac Fock–(RMCDF-) calculated hypersatellite x-ray spectra to the measured ones, Diamant *et al.* [14] concluded that within the experimental uncertainties the spectra for $23 \leqslant Z \leqslant 30$ elements are free from higher-order multivacancy contributions. On the other hand, the MCDF-based theoretical $K\alpha_{1,2}^h$ spectra for Al and Si reported by Costa *et al.* [35] yield FWHM linewidths of ∼2.4 eV that overestimate our experimental values.

It can also be questioned whether the natural widths of the singly ionized L shells can be used. The change in the central atomic potential (electronic relaxation) due to the K hole affects the L shell and even to a greater extent the outer-shell level binding energies. For valence electrons the solid state environment also plays an important role. It is well recognized that the Auger and Coster-Kronig decay rates depend strongly on small binding energy differences and the continuum-electron energies [45]. A typical example is the opening of the L_2-L_3X Coster-Kronig channels for the $3d$ transition metal solids, which are forbidden in free atoms [46,47]. Thus, considering that the lifetime of a vacancy is affected by additional holes present in the same level or in other levels, the K hypersatellite linewidth can be approximated as

$$\Gamma_{K\alpha^h} \cong \Gamma_{KK} + (\Gamma_{KL^{-1}} + \Gamma_{LK^{-1}}), \tag{3}$$

where $(\Gamma_{KL^{-1}} + \Gamma_{LK^{-1}})$ corresponds to the KL double-hole final-state width, and $\Gamma_{KL^{-1}}$ and $\Gamma_{LK^{-1}}$ denote the K and L level widths modified by the presence of an additional L, or, respectively, K vacancy. In Fig. 5(b) the $\Gamma_{L_2K^{-1}}$ values as derived from Eq. (3) are plotted vs Z and compared to the L_2 level widths of single-hole configuration states from [32]. The differences increase monotonically with Z up to $Z = 21$, undulate in the $22 \leqslant Z \leqslant 30$ region where the multiplet splitting effects are most prominent, and seem to diminish for Z around 40. For Ne, on the other hand, the measured width of the Auger KK-KLL hypersatellites of 1.0(1) eV [11] is consistent with the sum $\Gamma_{KK} + \Gamma_K + 2\Gamma_L$ of 1.08 eV.

Upon examining the reported differences between the experimental and calculated linewidths, it can be concluded that unless a drastic change in the decay rates of the KL double-hole final states is assumed, the experimental linewidths for $12 \leqslant Z \leqslant 30$ cannot be accounted for with the aid of the expression given by Eq. (3). Only elaborate relativistic MCDF calculations such as those of Chantler *et al.* [48] and the investigation of the effect of spectator vacancies on the L decay rates, in particular Auger widths that are predominant for low-Z elements, will permit resolution of the present discrepancies.

C. $I_{K\alpha_1^h}/I_{K\alpha_2^h}$ intensity ratios

Since for low-Z elements the $K\alpha_1^h$ transition is dipole forbidden in the pure L-S coupling scheme, x-ray emission occurs due to mixing between the $^3P_1$ and $^1P_1$ final configuration states. Thus, the hypersatellite $I_{K\alpha_1^h}/I_{K\alpha_2^h}$ intensity ratios probe the degree of intermediacy of the coupling and the various effects that influence the mixing, for instance Breit interaction and relativity. The present experimental $I_{K\alpha_1^h}/I_{K\alpha_2^h}$ intensity ratios are listed in Table II. For comparison data reported by other groups and theoretical predictions are included. Although for Mg and Al the $K\alpha_1^h$ x-ray transition was much too weak to be observed, it was measured for Si (see Fig. 2). The intensity ratio was found to be in excellent agreement with the MCDF theoretical predictions of Costa *et al.* [35] that include both the Breit and QED contributions. Indeed, these calculations predict that for elements $Z < 18$ the intensity ratio of the hypersatellite lines does not follow the same regular trend as that observed for $Z \geqslant 18$, but peaks at $Z = 15$. This effect is interpreted as being due to the interaction between the hole in the $2p$ level and the $3p$ electrons which opens several decay channels and leads to an increase of the $I_{K\alpha_1^h}/I_{K\alpha_2^h}$ intensity ratio. Unfortunately, due to the presence of the close-lying KMM radiative transitions, the $K\alpha_1^h$ x-ray line for Cl and K could not be extracted from the hypersatellite spectra (see Fig. 3). For Ca and Sc our data compare well within the experimental uncertainties with theory [35], but in the case of

V the calculations overestimate our result. The present ratio for V, however, agrees very closely with the experimental result of 0.08(1) and the RMCDF-calculated value of 0.077 reported by Diamant *et al.* [14].

IV. DOUBLE *K*-SHELL PHOTOIONIZATION

A. General considerations

Because a photon interacts with only one bound electron, double K-shell ionization following single-photon absorption is a clear manifestation of electron-electron interactions. Two mechanisms dominate the K-shell double photoionization, namely, the shake process and the inelastic electron-electron scattering (knockout). Shake-off (SO) is a purely quantum mechanical effect in which a sudden ejection of the photoelectron following photon absorption and a subsequent change of the atomic field lead to a removal of the remaining electron to the continuum. The double K-shell photoionization via shake is a consequence of the change of the self-consistent field and electron-electron correlations [49]. Knockout (KO) describes the correlated dynamics of a binary encounter in which the outgoing photoelectron knocks out the second $1s$ electron in an $(e,2e)$-like electron impact half collision [7]. In the shake-off process the total angular momentum of the system cannot change $\Delta L = 0$ (and $\Delta l = 0$), while conversely in electron-electron scattering an exchange of the angular momentum can take place. This would indicate that SO and KO lead essentially to different final atomic states. Further, ground-state electron correlations are important for the shake-off, while the final-state electron interactions govern the dielectronic process.

B. *Z* dependence

The double-to-single photoionization cross-section ratios in the region of the maximum of the photon energy evolution

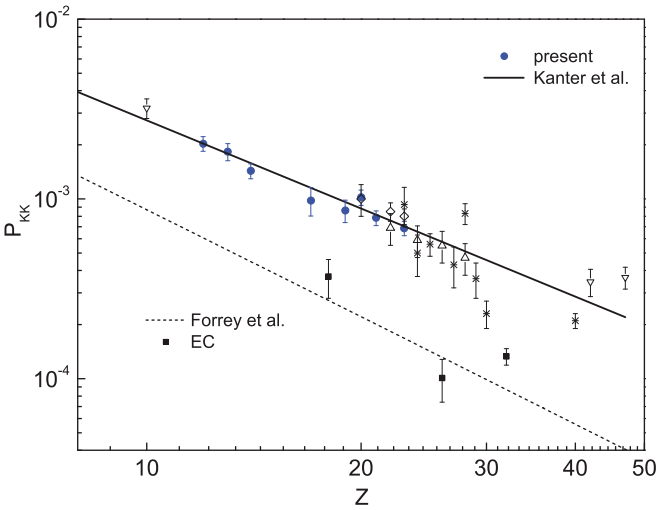

FIG. 6. (Color online) Double-to-single K-shell photoionization cross-section ratios versus atomic number. •, present results; ◇, [12]; ∗, [13,16]; △, [50]; ▽, [51]; ×, [7,52], and nuclear electron capture (EC) [53]. Photoabsorption asymptotic limits of Forrey *et al.* [54] (dashed line) and the power-law fit of Kanter *et al.* [15,51] (solid line) are also shown.

TABLE III. Double-to-single photoionization cross-section ratios in the peak region of the photon energy evolution. The ω_{KK}/ω_K were deduced from the values quoted by Chen [27].

Element	$P_{KK}^{\max}$	ω_{KK}/ω_K
Mg	$2.03(19) \times 10^{-3}$	1.27
Al	$1.83(20) \times 10^{-3}$	1.24
Si	$1.43(14) \times 10^{-3}$	1.21
Cl	$8.61(1.77) \times 10^{-4}$	1.12
K	$9.24(1.23) \times 10^{-4}$	1.087
Ca	$1.02(10) \times 10^{-3}$	1.08
Sc	$7.84(74) \times 10^{-4}$	1.075
V	$6.87(63) \times 10^{-4}$	1.065

$P_{KK}^{\max}$ are represented as a function of atomic number in Fig. 6 and listed in Table III. For comparison, other available experimental data are also plotted. The trend of our $P_{KK}^{\max}$ ratios is in good agreement with the weaker $1/Z^{1.6}$ dependence proposed by Kanter *et al.* [15,51], and all values lie above the asymptotic shake-off predictions of Forrey *et al.* [54], which follow the $1/Z^2$ falloff. Thus, our results suggest the predominance of KO in the broad maximum of the double-to-single photoionization cross-section ratios for low-Z elements, and confirm that the shake process alone cannot account for the double K-shell photoionization.

C. Photon energy dependence

The photon energy dependence of the double-to-single K-shell photoionization ratios P_{KK} for Mg, Al, Si, Ca, Sc, and V is presented in Fig. 7. The P_{KK} data sets cover wide photon beam energy ranges up to ∼2.8–3.3 the DPI threshold energies. It can seen that for all elements the P_{KK} ratio rises from threshold, reaches a broad maximum, and declines slowly with increasing photon energy. It is generally agreed that shake-off prevails at high photon energies, while knockout dominates near threshold and at intermediate energies. Indeed, the insensitivity of DPI to the ground-state correlations in the near-threshold region suggests a negligibly small SO contribution [21]. At intermediate photon energies it is difficult to isolate the two ionization processes unambigously [56]. As within *ab initio* calculations the SO and KO are treated coherently (see, e.g., [17,18,20,23,24,57]), alternative theoretical predictions based on an incoherent picture of the $(e,2e)$-like process and shake-off were proposed by Samson [58] and elaborated by Pattard and Burgdörfer [59]. In the same spirit, making use of the purely quantum nature of shake-off and through a quasiclassical formulation of the KO mechanism the separation of KO and SO processes with photon energy was achieved by Schneider *et al.* [19,60]. For He, an excellent agreement with experimental data and *ab initio* calculations for DPI from the ground state and also excited states [61] was obtained.

Recently, Hoszowska *et al.* [25] have investigated the role played by outer-shell electrons in the K-shell DPI [25]. To this end the phototoionization cross sections for hollow-K-shell Mg, Al, and Si atom production were compared to the convergent close-coupling calculations for the corresponding heliumlike ions. The experimental $P_{KK}^{\max}$ values for neutral

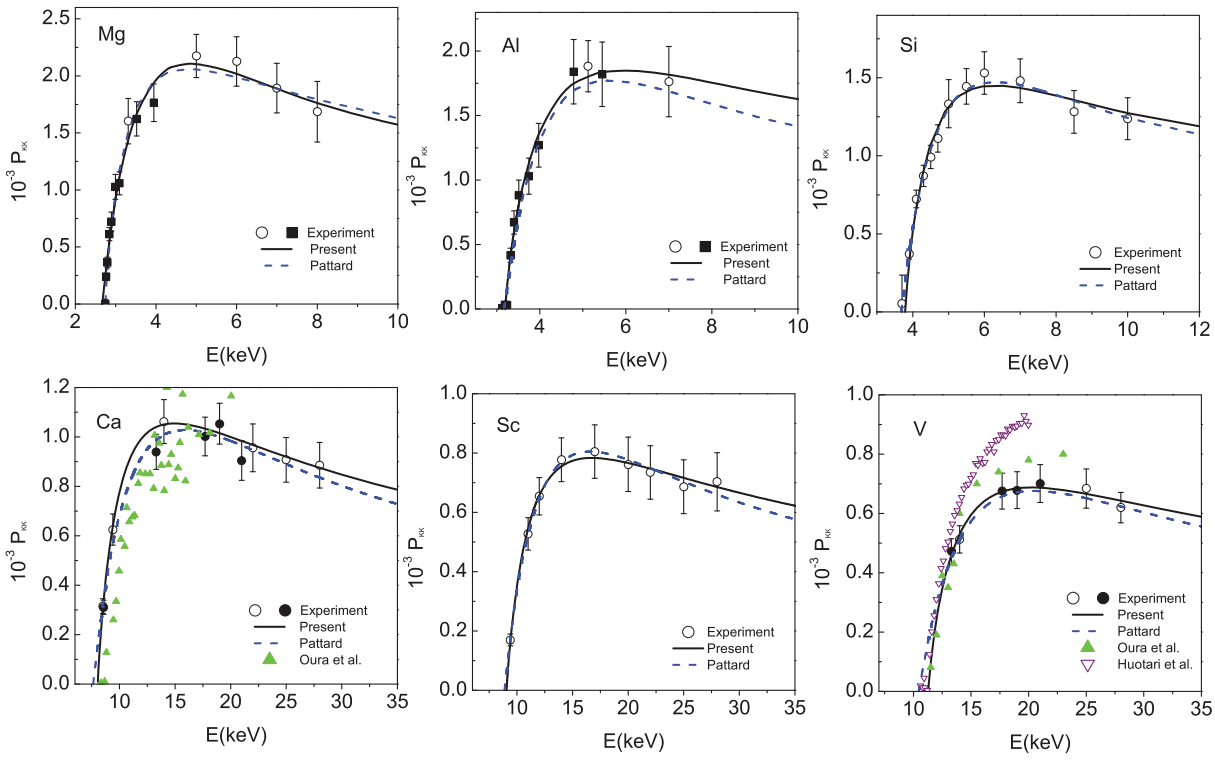

FIG. 7. (Color online) Double-to-single K-shell photoionization ratios P_{KK} for Mg, Al, Si, Ca, Sc, and V versus the photon beam energy. For Ca and V the present experimental data are compared to those of Oura *et al.* [12] and Huotari *et al.* [13]. Data recorded at the ID21 beamline are depicted by filled black rectangles, at the ID26 beamline by open black circles, and at the BM5 beamline by filled black circles. The solid black lines correspond to the best fits to our data with the SO-KO empirical model and the blue dashed lines show the fit with the analytical shape function of Pattard [55].

atoms were found systematically higher with respect to those of the two-electron ion counterparts, suggesting that the electron scattering contribution to DPI is more important for neutral atoms compared to the He isoelectronic series. To assess the effect of outer-shell electrons and the relative importance of final-state electron-electron correlations to the K-shell DPI, an SO-KO empirical model based on an incoherent summation of the double-to-single cross-section ratios for the shake process and knockout was proposed. In the following, the evolution of the double K-shell photoionization with the photon energy for $12 \leqslant Z \leqslant 23$ elements is investigated along these lines.

In our SO-KO empirical model the double-to-single photoionization ratio as a function of the photon energy is given by

$$P_{KK}(E) = P_{\mathrm{SO}}(E) + P_{\mathrm{KO}}(E), \tag{4}$$

with

$$P_{\mathrm{SO}}(E) = R_\infty \exp\left[-\frac{(rE^+)^2}{15.32(E-E^{2+})}\right] \tag{5a}$$

and

$$P_{\mathrm{KO}}(E) = P_{\mathrm{KO}}^{\max}\left\{\cosh\left(\beta \ln\left[\frac{E-E^{2+}}{\Delta E_{\mathrm{KO}}^{\max}}\right]\right)\right\}^{-\frac{1}{\beta}}. \tag{5b}$$

The $P_{\mathrm{SO}}(E)$ given by Eq. (5a) corresponds to the expression of Thomas [62] for shake-off. In this model, the transition from the adiabatic to the sudden regime is derived from time-dependent perturbation theory. Although to date at finite photon energies no unique definition exists for shake-off, different theoretical approaches including that of Thomas lead to essentially similar numerical results [49]. R_∞ stands for the shake-off asymptotic high-energy limit, i.e., when the photoelectron is infinitely fast, E^+ is the binding energy of the remaining K-shell electron, r represents the distance in angstroms traveled by the K photoelectron during the time the atomic potential changes, and E^{2+} denotes the DPI threshold energy. All energies are in eV.

For the knockout probability $P_{\mathrm{KO}}(E)$, the analytical form of the universal shape function for electron impact ionization of H-like ions of Aichele *et al.* [63] was adopted. Since the knockout in DPI describes a half collision between the ejected photoelectron and the residual ion, the choice of the shape function was based on the similarity of electron impact ionization of a H-like ion to the KO part of the double photoionization of the corresponding He-like ion [20,58–60]. Aichele *et al.* have shown that along the hydrogen isoelectronic sequence the experimental ionization cross sections σ_e scaled by their maximum values and plotted against the normalized excess energies $(E_e - I)/E_e^{\max}$ yield a universal curve. E_e stands for the incident electron energy and I is the ionization potential. Taking advantage of the fact that σ_e scales with the excess energy and that the KO contribution $P_{\mathrm{KO}}(E - E^{2+})$ is proportional to $\sigma_e(E_e - I)$, the universal shape function given by Eq. (5b) is readily obtained. The $P_{\mathrm{KO}}^{\max}$ corresponds to the maximum value of KO, $\Delta E_{\mathrm{KO}}^{\max}$ to

TABLE IV. Fitting parameters of the empirical SO-KO model. The DPI threshold energy E^{2+} and the $P_{\mathrm{KO}}^{\mathrm{max}}$ were derived from the fits, while R_∞ and E^+ were kept fixed. Also listed are the MCDF predictions for E^{2+}.

Element	Z	Z^*	E^{2+} (eV)	E^{2+} (eV)[a]	E^+ (eV)[a]	R_∞[b]	$P_{\mathrm{KO}}^{\mathrm{max}}$
Mg	12	10.4	2741(35)	2776.6	1464.8	6.08×10^{-4}	1.74×10^{-3}
Al	13	11.3	3189(23)	3294.0	1736.8	5.20×10^{-4}	1.55×10^{-3}
Si	14	12.2	3788(42)	3882.5	2032.5	4.47×10^{-4}	1.20×10^{-3}
Ca	20	17.8	8039(40)	8357.0	4324.7	2.22×10^{-4}	9.42×10^{-4}
Sc	21	18.8	9060(53)	9297.4	4791.8	2.00×10^{-4}	6.60×10^{-4}
V	23	20.7	11277(110)	11283.1	5798.7	1.68×10^{-4}	6.10×10^{-4}

[a]MCDF calculations.
[b]Photoabsorption asymptotic limits of Forrey *et al.* [54].

the excess energy where the maximum occurs, and the power $\beta = 0.4$.

In the fitting procedure only the E^+ values calculated with the GRASP code [64] and the asymptotic SO ratios R_∞ from [54] were kept fixed. Indeed, the shake-off asymptotic nonrelativistic high-energy limit is well understood in the framework of the sudden approximation [65]. Since in this approach the shake process results from the instantaneous change in the mean field, even in the absence of *e*-*e* correlations in the ground state, the sudden approximation yields nonzero shake probabilities. However, for electrons in the same shell, these are an order of magnitude too small. Therefore, provided that electron correlation is accounted for in the initial-state wave function, the shake-off in the high-energy limit can be calculated quite accurately for the helium isoelectronic sequence [54]. Mitnik and Miraglia [66] suggested that the influence of passive electrons on the ground-state correlations should be small. One can assume thus that R_∞ values for both neutral atoms and He-like ions are almost the same. The asymptotic double-to-single photoabsorption values for heliumlike ions Be^{2+} and Mg^{10+} are indeed close to those for neutral Be and Mg [24]. Further, as shown in Fig. 6, experimental data for double K-shell ionization following nuclear electron capture, which yield the double-to-single ratios corresponding to the shake process, agree with the predictions of Forrey *et al.* [54].

It should be noted that the sudden change of the atomic field upon photoelectron emission may also result in excitation of the remaining electron to an unoccupied bound state, i.e., shake-up (SU). Recently, Mukoyama [67] reported on the energy dependence of the shake process by taking into consideration the energy sharing between the photoelectron and the shake electron within the independent-particle sudden-approximation model. As according to these predictions for an initial K-shell core vacancy the SU contribution is less than 1.7% of the total shake probability for elements in the range $12 \leqslant Z \leqslant 23$ [68], it can be neglected.

Results of the least-squares fits to the experimental data with Eq. (4) are summarized in Table IV. The values for r decreased with increasing Z from ~0.09 to 0.05 Å. Experimental DPI threshold energies E^{2+} were found systematically lower compared to the MCDF predictions. Similar differences for the onset of DPI were reported for other elements [12,69]. The best fits to the double-to-single photoionization ratios as a function of the scaled excess energy are depicted in Fig. 8. For E^{2+} values from the fit were used, and the effective nuclear charge Z^* was deduced using the hydrogenic formula $E^+ = Z^{*2}\mathrm{Ry}$. It can be seen that the SO-KO model works quite well for all the elements. On inspection of Fig. 8 the prevalence of KO near threshold and for intermediate excess energies can be observed. At high excess energies KO becomes negligible and the P_{KK} ratios approach a constant value corresponding to the photoabsorption asymptotic limit of SO. Figure 8 also shows that the relative contribution of KO in the broad maximum of the double-to-single photoionization increases with Z. These results are in accordance with the conclusions of Kanter *et al.* [51] and Huotari *et al.* [13] for the predominance of KO near threshold and in the peak region of the P_{KK} photon energy evolution. The very good agreement between the experimental data for the photon energy dependence of P_{KK} and the SO-KO model fit suggests that the interference between KO and SO in the total DPI cross sections plays a minor role, and supports this simple physical picture for the K-shell double photoionization for low-Z neutral atoms.

It is also instructive to fit the data with the analytical formula for the double σ^{2+} to single σ^+ photoionization cross section ratio proposed by Pattard [55]:

$$\frac{\sigma^{2+}}{\sigma^+}(\Delta E) = R_\infty \frac{\Delta E^\alpha (\Delta E + E_0)^{7/2}}{(\Delta E + E_1)^{\alpha+7/2}}, \tag{6}$$

where ΔE is the excess energy, α stands for the Wannier threshold exponent [α varies smoothly from 1.056 ($Z = 2$) to 1.0 in the limit $Z \to \infty$], R_∞ is the asymptotic double-to-single photoabsorption ratio, and E_0 and E_1 are fit parameters. This shape function is based on the proposed analytical parametrization for ionization by bare projectiles [70], and it satisfies the Wannier law near threshold and the Bethe-Born theory at high energies. The fitted curves are shown as dashed lines in Fig. 7. In the fitting procedure R_∞ was fixed at values from Ref. [54]. While for He-like ions $E_0 \approx 2E_1$ holds, the E_0 parameters were found to be $\sim 2.5E_1$ for the experimental P_{KK} of Mg, Al, and Si and $\sim 2.7E_1$ for Ca, Sc, and V, respectively. These values are in contrast with the ones reported by Huotari *et al.* [13], who find E_0 almost equal to E_1. Indeed, only when we let R_∞ free in the fit do we find $E_0 \sim E_1$, but then R_∞ takes the value of $\sim P_{KK}^{\mathrm{max}}$. As illustrated in Fig. 7, the universal shape function by Pattard describes quite well the P_{KK} photon energy dependence for the studied elements. In comparison with the SO-KO model curves, the fit yields a slightly faster

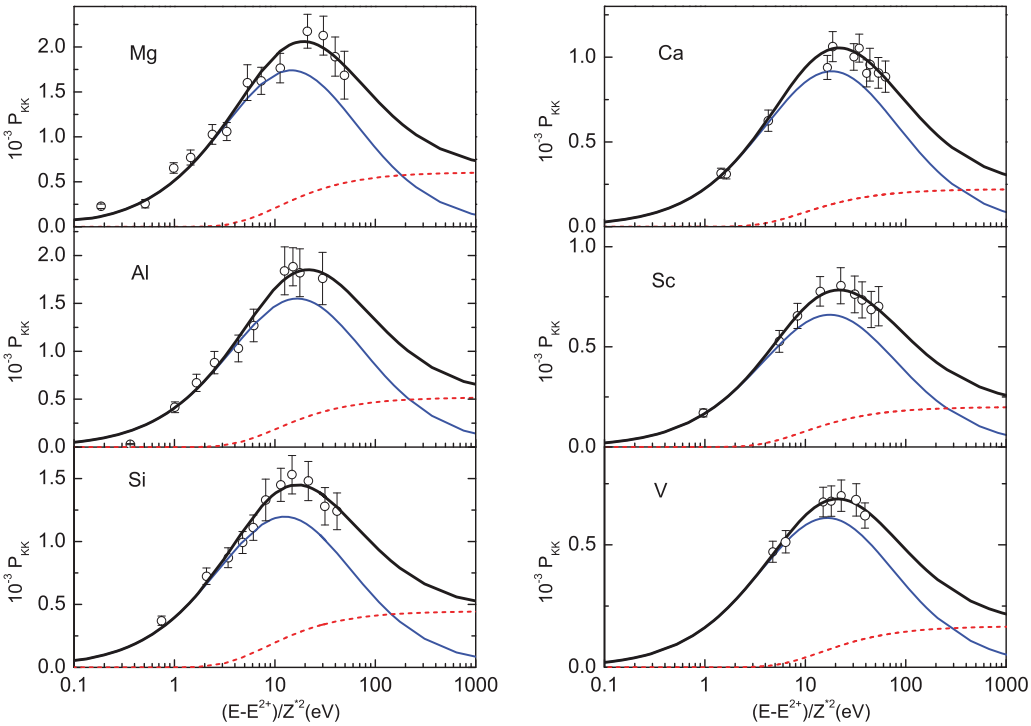

FIG. 8. (Color online) Double-to-single K-shell photoionization ratios as a function of the scaled excess energy. Results of best fits to our data with the SO-KO empirical model are represented by black solid thick lines, whereas the KO contribution is depicted by thin blue lines and the SO by red dashed lines.

decrease of P_{KK} toward the asymptotic limits and lowers by ∼2%–7% the DPI threshold energies.

D. Double-photoionization cross sections

The double K-shell photoionization cross sections were determined employing the relation

$$\sigma^{2+}(E) = P_{KK}(E)\sigma^{+}(E), \tag{7}$$

where E is the photon energy and σ^{+} stands for the single K-shell photoionization cross section deduced from the XCOM database [71]. Figure 9 illustrates the experimental DPI cross sections as a function of the photon energy. The cross sections have a common shape for all elements, characterized by a typical sharp rise above the onset for double ionization to the maximum $\sigma^{2+}_{\rm max}$ and a subsequent rapid decrease with increasing photon energy. Pattard [55] established a universal shape function for multiple ionization by photons that provides an excellent parametrization of photoionization cross sections in cases where all electrons are ionized. The proposed analytical formula of Pattard for double ionization of He-like ions reads

$$\sigma^{2+}(\Delta E) = \sigma^{2+}_{\rm max} x^{\alpha} \left[\frac{\alpha + 7/2}{\alpha x + 7/2}\right]^{(\alpha+7/2)}, \tag{8}$$

where $\sigma^{2+}_{\rm max}$ denotes the cross-section maximum, $\alpha = 1.056$, and $x = \Delta E/\Delta E^{\rm max}$. Both ΔE and $\Delta E^{\rm max}$ correspond to excess energies. To examine the applicability of the function beyond the simple systems we have fitted our DPI cross-section data with Eq. (8). The results of the least-squares fits are collected in Table V. The double-photoionization cross sections exhibit a maximum at ∼1.23 times the DPI threshold energies E^{2+}. The latter are consistent within the quoted errors with those obtained from the SO-KO model fits for Mg, Al, and Si. For higher-Z elements they are, however, slightly lower due to the limited number of experimental data points in the near-threshold region. The photon energies corresponding to the DPI cross-section maxima were found to follow the Z^{*2} dependence. More specifically, $E^{\rm max}(Z^*) = 25.03(11)Z^{*2.08(3)}$ and the excess energies $\Delta E^{\rm max}(Z^*) = 5.72(0.07)Z^{*2.00(7)}$. As illustrated in Fig. 9, the universal shape function of Pattard is found to be applicable to K-shell hollow atoms as well.

V. SCALING LAWS

It is worthwhile to ask whether the scaling properties of DPI cross sections and the double-to-single photoionization cross-section ratios for two-electron systems suggested by Kornberg and Miraglia [72] hold for neutral atoms. First we examine the double-to-single cross-section ratios. Indeed, the scaled $P_{KK}/P^{\rm max}_{KK}$ values fall on one curve if plotted as a function of the scaled excess energy. This common shape also coincides from threshold up to the maximum with the universal curve of Huotari *et al.* [13]. Note that data by Huotari *et al.* do not extend beyond the P_{KK} broad maximum. However, in view of the weaker Z dependence of $P^{\rm max}_{KK}$ for neutral atoms of $Z^{-1.61(5)}$ [15,51], one should not expect the double-to-single photoionization cross-section ratios to obey the scaling relation with Z^{*2} which is valid for the He isoelectronic sequence [60]. Indeed, Fig. 10 illustrates that the scaled double-to-single photoionization cross-section ratios for neutral elements do not fall on one curve.

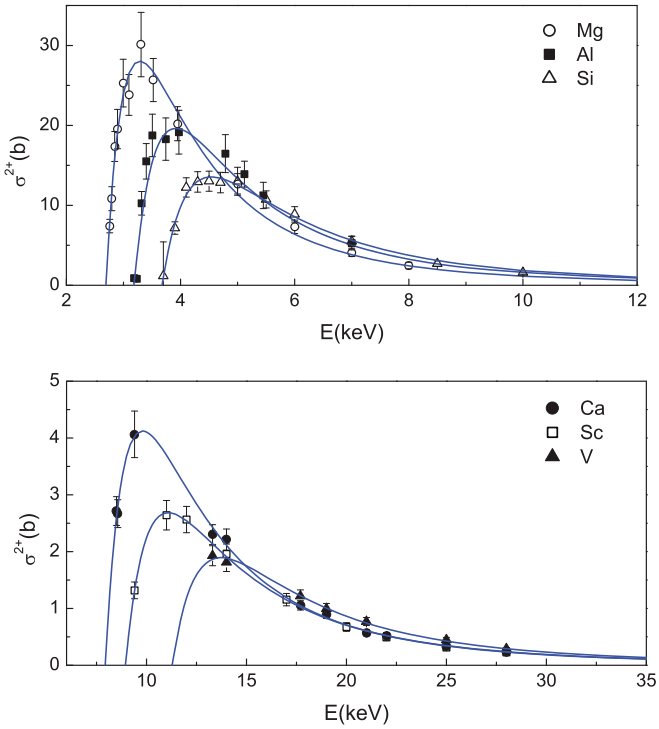

FIG. 9. (Color online) Double K-shell photoionization cross sections for Mg, Al, and Si (upper panel), and Ca, Sc, and V (lower panel). Solid lines show the best fits with the universal shape function of Pattard [55].

Noteworthy is the similar evolution for each of the studied elements of the knockout and shake-off as a function of the excess energy scaled with Z^*, i.e., the remaining electron binding energy (see Fig. 8). This feature reflects the fact that the many-electron response to single photoabsorption takes place prior to the subsequent secondary electron emission mediated by the KO process. In the case of shake-off, one can speculate that in the high-energy limit the remaining K-shell electron has no time to adjust to the sudden potential change. It is shaken off into continuum due to the sudden perturbation at the moment of the departure of the first electron, the SO probability depending strongly on the intrashell electron correlations. For low excess energies, however, one can argue that the K-shell electron is shaken off during the relaxation time of the core-excited atom after photoelectron ejection. Indeed, this is in line with the

TABLE V. Fitting parameters of the shape function by Pattard [55] for the double-photoionization cross sections. The $\sigma^{2+}_{\rm max}$ are in units of barns. The quoted uncertainties of $\sigma^{2+}_{\rm max}$ include both the experimental and statistical errors, where for σ^+ relative uncertainties of 5% were assumed. For V, the E^{2+} was fixed at the value from Table IV.

Element	$\sigma^{2+}_{\rm max}$ (b)	$E^{\rm max}$ (eV)	E^{2+} (eV)
Mg	28.0(1.4)	3286(33)	2693(13)
Al	19.7(2.9)	3913(54)	3183(17)
Si	13.6(1.3)	4542(28)	3674(11)
Ca	4.1(0.5)	9798(48)	7933(39)
Sc	2.68(0.3)	11094(36)	8942(20)
V	1.89(0.7)	13722(57)	11277

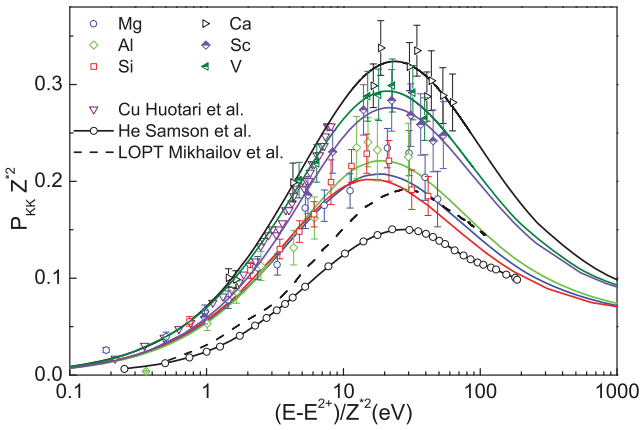

FIG. 10. (Color online) Scaled experimental double-to-single photoionization cross-section ratios versus the scaled excess energy. The solid lines represent the SO-KO model fit. The experimental data for He are from Samson *et al.* [7] and for Cu from Huotari *et al.* [13]. The dashed line corresponds to the LOPT calculations of Mikhailov *et al.* [23].

definition of SO in the adiabatic regime formulated by Thomas [62]. Resorting to the adiabaticity parameter $t_0 E^+/\hbar$, one finds t_0 as the time the potential changes, or the characteristic time for the emission process. Thus, knowing the mean distance r traveled by the ejected photoelectron from the SO-KO model fit, a rough estimate of the time scale of the many-electron interactions leading to the change in the atomic field in the adiabatic SO regime is at hand. For instance, at an excess energy corresponding to the maxima of the $P_{\rm KO}$ photon energy dependencies, t_0 amounts to ∼2.6 as and ∼0.1 as, for Mg and V, respectively. The observed behavior of KO and SO with the scaled excess energy could imply only small differences in the time scales for the second 1s electron ejection via KO and SO at low excess energies. To the best of our knowledge, this

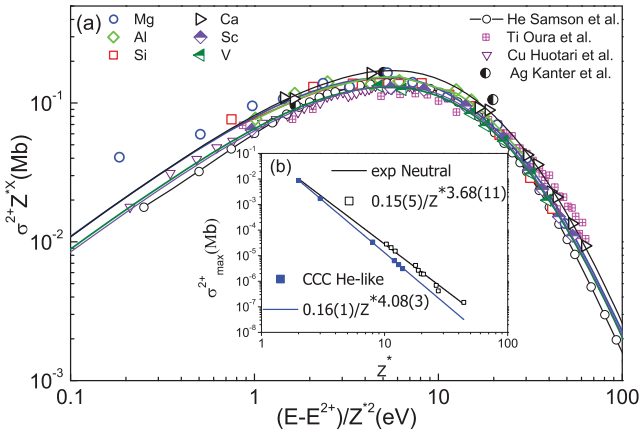

FIG. 11. (Color online) (a) Scaled experimental DPI cross sections for Mg, Al, Si, Ca, Sc, and V compared to the scaled data for He [7] and experimental data for higher-Z elements Ti [12], Cu [13], and Ag [51] as a function of the scaled excess energy. A scaling exponent X of 3.68 for neutral atoms was used (see inset). The curves (solid lines) were deduced from the fitted values of P_{KK} shown in Fig. 8. (b) Shown are the power-law fits to the maximum values of σ^{2+} as a function of Z^*. The error bars are smaller than the symbols.

aspect of single-photon DPI of neutral atoms remains elusive to date, and certainly deserves future investigation.

Recently we have established a semiempirical universal scaling of the double-photoionization cross sections with the effective nuclear charge [25]. To this end, first power-law fits to the maximum values of σ^{2+} as a function of Z^* were performed. As expected, for He-like ions a $Z^{*-4.08(3)}$ falloff was found; however, for neutral atoms a $Z^{*-3.68(11)}$ dependence was determined [see Fig. 11(b)]. As depicted in Fig. 11(a), the scaled double -photoionization cross sections for Mg, Al, Si, Ca, Sc, and V in reduced coordinates $\sigma^{2+}Z^{*3.68}$ against $(E - E^{2+})/Z^{*2}$ collapse onto a single curve. Further, the $\sigma^{2+}Z^{*3.68}$ data for neutral atoms in the range $2 \leqslant Z \leqslant 47$, within the experimental uncertainties, exhibit a universal scaling behavior and coincide with $\sigma^{2+}Z^{*4}$ for the He isoelectronic series.

VI. SUMMARY AND CONCLUDING REMARKS

In summary, the single-photon K-shell hollow atom production and radiative decay via K x-ray hypersatellites for the $12 \leqslant Z \leqslant 23$ range was investigated. Monochromatic synchrotron radiation and the high-resolution x-ray emission spectroscopy technique were employed. Energies and linewidths of the $K\alpha^h$ hypersatellite x-ray transitions, and the $K\alpha_1^h$:$K\alpha_2^h$ intensity ratios were determined and compared to calculations as well as to other experimental data. A good to excellent agreement between the experimental and theoretical K hypersatellite energies was found. Conversely, open questions remain for the linewidths of the $K\alpha^h$ hypersatellite x-ray transitions. The reported discrepancies with the calculated values point to a need for elaborate MCDF calculations and also examination of the effect of spectator vacancies on the L-shell decay rates.

Our main goal was to shed light on electron-electron interaction effects in the single-photon double-K-vacancy production. With this objective in mind, the photon energy dependencies of the double-to-single photoionization cross-section ratios were determined over wide photon energy ranges from the DPI thresholds up to and beyond the maxima. To evince the relative importance of the initial-state and final-state electron-electron interactions to the K-shell double photoionization, an approach based on an incoherent summation of the knockout and shake-off mechanisms of the K-shell DPI process was applied [25]. Our findings are in accord with the conclusions of Kanter *et al.* [51] and Huotari *et al.* [13] for the prevalence of the postphotoabsorption electron correlations in the near-threshold region and for intermediate photon energies.

Finally, the Z-dependent trends and scaling properties of the double-to-single photoionization cross-section ratios and the DPI cross sections were assessed. The universal shape functions of Pattard [55] were found to be applicable. Further, we have shown that the Z^{*2} scaling of the K-shell double-to-single photoionization cross-section ratios for neutral atoms breaks down. In contrast, it was demonstrated that a semiempirical universal scaling of the double-photoionization cross sections with the effective nuclear charge $Z^{*3.68}$ does hold for neutral atoms from He ($Z = 2$) to Ag ($Z = 47$). We hope that the reported results and findings have brought additional insights, and will stimulate further theoretical work on the double photoionization of neutral atoms.

ACKNOWLEDGMENTS

We wish to acknowledge the support of the Swiss National Science Foundation and the ESRF.

[1] J. H. McGuire, N. Berrah, R. J. Bartlett, J. A. R. Samson, J. A. Tanis, C. L. Cocke, and A. S. Schlachter, J. Phys. B **28**, 913 (1995).
[2] J. S. Briggs and V. Schmidt, J. Phys. B **33**, R1 (2000).
[3] R. Dörner, H. Schmidt-Böcking, T. Weber, M. Schöffler, T. Jahnke, A. Knapp, M. Hattass, A. Czasch, L. Ph. H. Schmidt, and O. Jagutzki, Radiat. Phys. Chem. **70**, 191 (2004).
[4] L. Avaldi and A. Heutz, J. Phys. B **38**, S861 (2005).
[5] J. P. Briand, Phys. Rev. Lett. **27**, 777 (1971).
[6] G. Charpak, C. R. Hebd. Seances Acad. Sci. **237**, 243 (1953).
[7] J. A. R. Samson, W. C. Stolte, Z.-X. He, J. N. Cutler, Y. Lu, and R. J. Bartlett, Phys. Rev. A **57**, 1906 (1998).
[8] R. Wehlitz, M. M. Martinez, J. B. Bluett, D. Lukić, and S. B. Whitfield, Phys. Rev. A **69**, 062709 (2004).
[9] O. Keski-Rahkonen, J. Saijonmaa, M. Suvanen, and A. Servomaa, Phys. Scr. **16**, 105 (1977).
[10] E. Mikkola and J. Ahopelto, Phys. Scr. **27**, 297 (1983).
[11] S. H. Southworth, E. P. Kanter, B. Krässig, L. Young, G. B. Armen, J. C. Levin, D. L. Ederer, and M. H. Chen, Phys. Rev. A **67**, 062712 (2003).
[12] M. Oura *et al.*, J. Phys. B **35**, 3847 (2002).
[13] S. Huotari, K. Hämäläinen, R. Diamant, R. Sharon, C. C. Kao, and M. Deutsch, Phys. Rev. Lett. **101**, 043001 (2008).
[14] R. Diamant, S. Huotari, K. Hämäläinen, R. Sharon, C. C. Kao, and M. Deutsch, Phys. Rev. A **79**, 062511 (2009).
[15] E. P. Kanter, R. W. Dunford, B. Krässig, and S. H. Southworth, Phys. Rev. Lett. **83**, 508 (1999).
[16] S. Huotari, K. Hämäläinen, R. Diamant, R. Sharon, C.-C. Kao, and M. Deutsch, J. Electron Spectrosc. Relat. Phenom. **137**, 293 (2004).
[17] K. I. Hino, T. Ishihara, F. Shimizu, N. Toshima, and J. H. McGuire, Phys. Rev. A **48**, 1271 (1993).
[18] J. Colgan, M. S. Pindzola, and F. Robicheaux, J. Phys. B **34**, L457 (2001).
[19] T. Schneider, P. L. Chocian, and J. M. Rost, Phys. Rev. Lett. **89**, 073002 (2002).
[20] A. S. Kheifets, J. Phys. B **34**, L247 (2001).
[21] A. S. Kheifets and I. Bray, Phys. Rev. A **57**, 2590 (1998).
[22] A. S. Kheifets and I. Bray, Phys. Rev. A **58**, 4501 (1998).
[23] A. I. Mikhailov, I. A. Mikhailov, A. N. Moskalev, A. V. Nefiodov, G. Plunien, and G. Soff, Phys. Rev. A **69**, 032703 (2004).
[24] A. S. Kheifets, I. Bray, and J. Hoszowska, Phys. Rev. A **79**, 042504 (2009).
[25] J. Hoszowska *et al.*, Phys. Rev. Lett. **102**, 073006 (2009).

[26] J. Hoszowska, J.-Cl. Dousse, J. Kern, and Ch. Rhême, Nucl. Instrum. Methods Phys. Res. A **376**, 129 (1996).
[27] M. H. Chen, Phys. Rev. A **44**, 239 (1991).
[28] F. Bloch and P. A. Ross, Phys. Rev. **47**, 884 (1935).
[29] T. Åberg and J. Utriainen, Phys. Rev. Lett. **22**, 1346 (1969).
[30] J. Szlachetko, J.-Cl. Dousse, J. Hoszowska, M. Berset, W. Cao, M. Szlachetko, and M. Kačič, Rev. Sci. Instrum. **78**, 093102 (2007).
[31] R. D. Deslattes, Jr. E. G. Kessler, P. Indelicato, L. de Billy, E. Lindroth, and J. Anton, Rev. Mod. Phys. **75**, 35 (2003).
[32] J. L. Campbell and T. Papp, At. Data Nucl. Data Tables **77**, 1 (2001).
[33] K. Fennane, J.-Cl. Dousse, J. Hoszowska, M. Berset, W. Cao, Y.-P. Maillard, J. Szlachetko, M. Szlachetko, and M. Kavčič, Phys. Rev. A **79**, 032708 (2009).
[34] M. C. Martins, A. M. Costa, J. P. Santos, F. Parente, and P. Indelicato, J. Phys. B **37**, 3785 (2004).
[35] A. M. Costa, M. C. Martins, J. P. Santos, P. Indelicato, and F. Parente, J. Phys. B **40**, 57 (2007).
[36] L. Natarajan, Phys. Rev. A **78**, 052505 (2008).
[37] E. Mikkola, O. Keski-Rahkonen, and R. Kuoppala, Phys. Scr. **19**, 29 (1979).
[38] M. Kavčič and K. Tökési, Phys. Rev. A **72**, 062704 (2005).
[39] J. P. Mossé, P. Chevalier, and J. P. Briand, Z. Phys. A **322**, 207 (1985).
[40] R. Diamant, S. Huotari, K. Hämäläinen, C. C. Kao, and M. Deutsch, Phys. Rev. A **62**, 052519 (2000).
[41] F. P. Larkins, J. Phys. B **4**, L29 (1971).
[42] D. F. Anagnostopoulus, J. Phys. B **28**, 47 (1995).
[43] Y. Kayser, M.S. thesis, Fribourg University, 2007.
[44] B. Boschung *et al.*, Phys. Rev. A **51**, 3650 (1995).
[45] L. I. Yin, I. Adler, M. H. Chen, and B. Crasemann, Phys. Rev. A **7**, 897 (1973).
[46] J. A. D. Matthew, J. D. Nuttall, and T. E. Gallon, J. Phys. C **9**, 883 (1976).
[47] J. L. Campbell and T. Papp, X-ray Spectrom. **24**, 307 (1995).
[48] C. T. Chantler, A. C. L. Hayward, and I. P. Grant, Phys. Rev. Lett. **103**, 123002 (2009).
[49] T. Pattard, T. Schneider, and J. M. Rost, J. Phys. B **36**, L189 (2003).
[50] J. Ahopelto, E. Rantavuori, and O. Keski-Rahkonen, Phys. Scr. **20**, 71 (1979).
[51] E. P. Kanter, I. Ahmad, R. W. Dunford, D. S. Gemmell, B. Krässig, S. H. Southworth, and L. Young, Phys. Rev. A **73**, 022708 (2006).
[52] L. Spielberger *et al.*, Phys. Rev. Lett. **74**, 4615 (1995).
[53] A. Suzuki and J. Law, Phys. Rev. C **25**, 2722 (1982).
[54] R. C. Forrey, H. R. Sadeghpour, J. D. Baker, J. D. Morgan, and A. Dalgarno, Phys. Rev. A **51**, 2112 (1995).
[55] T. Pattard, J. Phys. B **35**, L207 (2003).
[56] A. Knapp *et al.*, Phys. Rev. Lett. **89**, 033004 (2002).
[57] A. S. Kheifets, D. V. Fursa, and I. Bray, Phys. Rev. A **80**, 063413 (2009).
[58] J. A. R. Samson, Phys. Rev. Lett. **65**, 2861 (1990).
[59] T. Pattard and J. Burgdörfer, Phys. Rev. A **64**, 042720 (2001).
[60] T. Schneider and J.-M. Rost, Phys. Rev. A **67**, 062704 (2003).
[61] A. Emmanoulidou, T. Schneider, and J.-M. Rost, J. Phys. B **36**, 2717 (2003).
[62] T. D. Thomas, Phys. Rev. Lett. **52**, 417 (1984).
[63] K. Aichele, U. Hartenfeller, D. Hathiramani, G. Hofmann, V. Schäfer, M. Steidl, M. Stenke, E. Salzborn, T. Pattard, and J. M. Rost, J. Phys. B **31**, 2369 (1998).
[64] K. G. Dyall, I. P. Grant, C. T. Johnson, F. A. Parpia, and E. P. Plummer, Comput. Phys. Commun. **55**, 425 (1989).
[65] T. Mukoyama and K. Taniguchi, Phys. Rev. A **36**, 693 (1987).
[66] D. M. Mitnik and J. E. Miraglia, J. Phys. B **38**, 3325 (2005).
[67] T. Mukoyama, X-ray Spectrom. **39**, 142 (2010).
[68] T. Mukoyama (private communication).
[69] R. Diamant, S. Huotari, K. Hämäläinen, C. C. Kao, and M. Deutsch, Phys. Rev. Lett. **84**, 3278 (2000).
[70] J. M. Rost and T. Pattard, Phys. Rev. A **55**, R5 (1997).
[71] [http://physics.nist.gov/xcom].
[72] M. A. Kornberg and J. E. Miraglia, Phys. Rev. A **49**, 5120 (1994).